

# Inference on binary images from binary data

C.A. Glasbey

Biomathematics and Statistics Scotland

JCMB, King's Buildings, Edinburgh, EH9 3JZ, Scotland

*Abstract* – The problem addressed is to reverse the degradation which occurs when images are digitised: they are blurred, subjected to noise and rounding error, and sampled only at a lattice of points. Inference is considered for the fundamental case of binary scenes, binary data and isotropic blur. The inferential process is separable into two stages: first from the lattice points to a binary image in continuous space and then the reversal of thresholding and blur. Methods are motivated by, and illustrated using, an electron micrograph of an immunogold-labelled section of tulip virus.

# 1 Introduction

Digital images are imperfect representations of reality. Typically, data are affected by blur, subjected to noise and rounding error, and sampled only at a lattice of points. A fundamental case is where the true scene is binary, and the data are also binary, because either the digitising sensor is binary or blur is minimal.

To illustrate, Fig 1 shows an electron micrograph of a section of pellet of purified tulip virus X which has been immunogold labelled with antiserum (Roberts, 1994). In comparison, Fig 2 shows a binary digitisation of Fig 1 at a coarse spatial resolution, such as would be produced by a binary digitising sensor. (Here and in subsequent figures we follow the convention of displaying pixels as contiguous squares rather than as distinct points on a grid. For the moment ignore the distinction between grey and black pixels). Fig 1 can be thought of as a blurred and noisy version of a binary scene, consisting of black discs (which are the gold particles) on a grey background. The particles are distributed at random, except for local clustering effects where two or three particles are drawn together by surface tension, and they are spherical in shape, with radii which are normally distributed with mean  $\mu = 6.5$  nm, standard deviation  $\sigma = 0.41$  nm. Further, the blur is Gaussian with standard deviation  $\tau = 1.4$  nm. (We will not go into details of how these values were obtained.) Fig 2 is sampled at one pixel per 8.5 nm, with the binary threshold set at a value 25% of the way between the foreground and background levels in Fig 1. The threshold between white and black ensures that all black pixels are due to gold particles. We would like to use Fig 2 rather than Fig 1 to count the number, and estimate the size distribution, of the gold particles.

We will return to this example for motivation and illustration, but will consider the problem in greater generality. We assume that the effects of noise can be neglected, i.e. sampling variation is much less than the effects of thresholding. This is often a reasonable assumption to make with binary data, and the inferential problem would be significantly harder without it. We also assume that the blur of known form, because otherwise there is insufficient information to estimate it from binary data except in very restrictive circumstances. We will restrict attention to square lattices, although the results are generalisable to rectangular, hexagonal and other configurations. Therefore, as has been stated by many earlier authors, the data are an array of pixels,  $z_{ij}$ , for integer lattice positions  $(i, j)$ , such that

$$z_{ij} = \begin{cases} 1 & \text{if } \left\{ \int_{-\infty}^{+\infty} f(x, y) g(x - i, y - j) dx dy \right\} \leq T \\ 0 & \text{otherwise.} \end{cases}$$

Here,  $T$  is a known threshold,  $g$  is the blurring function and  $f(x, y)$  is the intensity

of the binary scene at 2D location  $(x, y)$ :

$$f(x, y) = \begin{cases} f_1 & \text{if } (x, y) \in C \\ f_0 & \text{otherwise,} \end{cases}$$

for some set  $C$  and known foreground and background levels of  $f_1$  and  $f_0$ . The values of 0 and 1 for  $z$  will henceforth be referred to as white and black, respectively.

The problem to be addressed in this paper is one of inferring  $f$  from  $z$ . The positioning of the image with respect to the sampling lattice is assumed to be random in both location and orientation. By restricting attention to isotopic blur, the positioning of the integer lattice can be considered separately from the effect of blurring and thresholding. So, if we define  $\tilde{f}$  by

$$\tilde{f}(u, v) = \begin{cases} 1 & \text{if } \left\{ \int_{-\infty}^{+\infty} f(x, y) g(x - u, y - v) dx dy \right\} \leq T \\ 0 & \text{otherwise,} \end{cases}$$

for  $(u, v) \in \mathbb{R}^2$ , then  $z_{ij} = \tilde{f}(i, j)$ , and we can infer  $\tilde{f}$  from  $z$ , followed by  $f$  from  $\tilde{f}$ . In §2, the first stage in the restoration process will be considered, that of inferring a binary image in continuous space ( $\tilde{f}$ ) from lattice data ( $z$ ). Then, in §3, inference on  $f$  from its blurred, thresholded version ( $\tilde{f}$ ) will be discussed. (If blur is absent, then  $g$  is a delta-function,  $\tilde{f}(u, v) \propto f(u, v)$ , and the second stage can be omitted.) In the terminology of Grenander's (1976) pattern theory, §2 is an example of 'incomplete data' and §3 of 'indirect data'.

As far as I am aware this particular problem has not been considered before, although it has close connections with work in several other areas, including image digitisation, number theory, stochastic geometry, mathematical morphology, image restoration and printing/lithography. Digital representations of simple geometric shapes such as straight lines (Dorst and Duin, 1984) and circles (Nakamura and Aizawa, 1984) have been analysed. Also the information loss due to both spatial and intensity quantisation has been studied by Nielsen *et al* (1984) and Bruckstein (1987). Havelock (1989, 1991) considered the precision with which a point could be located in continuous space, given lattice observations of a blurred version subject to rounding errors, including binary data as a special case. The number of lattice points lying within a randomly positioned circle is a classical problem in number theory which continues to generate interest (see, for example, Bleher *et al*, 1993). Asymptotic results have also been obtained for other shapes, such as ovals (Kendall, 1948) and parallelograms (Holgate, 1990). See also Kendall and Moran (1962, chapter 5) and the more general theory of combinatorial stochastic geometry (Ambartzumian, 1981). A major contribution to the analysis of binary images, including some aspects of the relationship between lattice-based and continuous representations, has been mathematical morphology, developed by Serra (1982,

1988) and co-workers. For example, Minkowski sum and difference operators can be used to analyse the effects of lattice translations on the pixel representation of objects (Serra, 1992, p 225). Many approaches to the restoration of grey-level images have been considered (Rosenfeld and Kak, 1982, chapter 7), including recovery to sub-pixel accuracy (Koplowitz and Raj, 1987; Sriraman *et al*, 1989; Boulton and Wolberg, 1993). Bayesian methods with global priors have been used by Ripley (1991) and Aykroyd and Green (1991), among others. Davies (1990, chapter 9) considered circle detection in the context of machine vision. Korostelev and Tsybakov (1993) and Rudemo and Stryhn (1994) derived estimators, with asymptotic efficiencies, of a boundary fragment in a binary image observed subject to noise. Saleh (1987) considered some algorithms for reversing blur in binary images, particularly from a printer's perspective of constructing a binary function,  $f$ , such that its blurred version,  $\tilde{f}$ , is of a prescribed form. The results also have applications in microlithography (Fu *et al*, 1991).

## 2 Lattice sampling

Let  $\tilde{C}$  denote the set of points  $(x, y)$  for which  $\tilde{f}(x, y) = 1$ . In §2.1 it is assumed that  $\tilde{C}$  is a disc. Maximum likelihood estimators of disc size are derived for observed groups of black pixels, and in §2.2 these results are applied to Fig 2. Maximum likelihood estimators of elliptical and polygonal sets are obtained by simulation in §2.3. Finally, in §2.4 it is shown that a disc is not (as might be expected) the set which maximises the probability of observing a single black pixel, and it remains an open question as to what is.

### 2.1 Disc sets

The problem is similar to that of 'franc-carreau', considered by Buffon in 1777 (see Solomon, 1978, p 1). However, he was concerned with the number of square tiles overlapped by a disc, whereas we are interested in counting the number of intersections of four tiles or, equivalently, the number of tile centres. If the radius ( $r$ ) of  $\tilde{C}$  is less than 0.5, then at most one lattice point can lie inside it. Given random positioning of the disc with respect to the sampling lattice, the probability of observing a single black pixel is equal to the disc area, that is

$$P_1(r) = \pi r^2.$$

If  $0.5 \leq r \leq \sqrt{0.5}$ , then zero, one or two adjacent pixels may be observed. It is only necessary to consider the position of the disc centre within a single square in

the lattice. Fig 3 shows how the square is partitioned, an example of the locales considered by Havelock (1989). If the centre of the disc lies in a region labelled 1, then a single black pixel is observed. Similarly 0, 2 pixels are observed if the disc centre lies in regions labelled 0, 2 respectively. It follows that the probability of observing 2 black pixels is

$$P_2(r) = 8 \left( \frac{\alpha r^2}{2} - \frac{1}{4} \sqrt{r^2 - \frac{1}{4}} \right) = 4\alpha r^2 - \sqrt{4r^2 - 1},$$

where  $\alpha = \cos^{-1} \frac{1}{2r}$ . Similarly,

$$P_1(r) = \pi r^2 - 2P_2(r) = \pi r^2 - 8\alpha r^2 + 2\sqrt{4r^2 - 1}.$$

If  $\sqrt{0.5} \leq r \leq 1$ , then between one and four lattice points can lie within the disc. The algebra becomes more complicated, but in particular

$$P_1(r) = z^2 + z\sqrt{4r^2 - z^2} - 4r^2 \sin^{-1} \frac{z}{2r},$$

where  $z = 1 - \sqrt{2r^2 - 1}$ . For  $r > 1$ , the algebraic manipulations necessary to evaluate the probabilities of different configurations of black pixels becomes progressively more complicated. It is easier to numerically integrate over locations of disc centres. Fig 4 shows the results for a range of disc areas.

For each observed pattern of pixels, it is possible to derive the size of disc most likely to have produced it, i.e. the maximum likelihood estimate conditional on  $\tilde{C}$  being a disc. The left-most two columns in Fig 5 show the observed black pixels and estimated discs. In these results, rotations and reflections of patterns of pixels have not been counted as distinct. Some patterns, such as diagonally adjacent pixels, cannot be produced by a disc and so have been left blank. For a single pixel, the maximum value of  $P_1(r)$  occurs when  $0.5 \leq r \leq \sqrt{0.5}$ , and

$$\frac{dP_1}{dr} = 2\pi r - 16\alpha r - \frac{8r^2}{2r\sqrt{r^2 - \frac{1}{4}}} + \frac{8r}{\sqrt{4r^2 - 1}}$$

which equals 0 when  $\alpha = \frac{\pi}{8}$ . Therefore, at the maximum,

$$\hat{r} = \frac{1}{2 \cos \frac{\pi}{8}} = \frac{1}{\sqrt{2 + \sqrt{2}}} = 0.541,$$

the disc area is 0.92 and  $P_1(\hat{r}) = 82.8\%$ . It is perhaps surprising that a disc of unit area does not maximise the probability of observing a single pixel. A 95% confidence interval for the radius is given by values for which  $P_1(r) \geq 0.828 \times e^{-1.92}$ , i.e.  $0.20 \leq r \leq 0.83$ . The width of the interval illustrates the imprecision of inference from binary data. However, we can do better with larger numbers of observations, as we show in the next section.

## 2.2 Example

We restrict attention to 4-connected groups of pixels, as is appropriate for discs. The 7 grey areas in Fig 2 were identified as being produced by groups of two or more gold particles. In 6 cases this was because the pattern of pixels could not have been produced by a single disc. In the final case, the group of 5 pixels in the centre-left of the figure, the disc would have had to have been larger than the permitted range of radii of gold particles. There remain 99 groups of one or more black pixels, which we assume are each due to a single gold particle. The observed size distribution is given in Table 1. If the particles have normally distributed radii, then the parameters can be estimated numerically by maximising the likelihood. Expected frequencies are obtained by convolving the probability curves in Fig 4 with the normal distribution. The mean is estimated as  $\hat{\mu} = 5.8$  nm, with a standard error of 0.14 nm obtained from the observed information matrix in the standard way, and the standard deviation is  $\hat{\sigma} = 0.57$  nm (s.e. 0.20). The fit is good, as can be seen in the agreement between observed and expected values in Table 1. The parameter estimates cannot be compared directly with those given in §1, because the effects of blur and thresholding have not yet been allowed for (see §3.1).

Table 1: Observed and expected size groups in Fig 2, and the maximum likelihood fit of a normal distribution to gold particle radii.

number of pixels	0	1	2	3	4
observed	*	50	46	3	0
expected	1.5	49.9	46.4	2.2	0.6

\* denotes a missing value

The mean area of  $\tilde{C}$  is  $\pi(\hat{\mu}^2 + \hat{\sigma}^2) = 108$  nm<sup>2</sup> and the sampling rate is one pixel per 8.5<sup>2</sup> nm<sup>2</sup>. Therefore, the 33 grey pixels in Fig 2 are expected to represent  $33 \times 8.5^2 / 108 = 21.9$  gold particles, on the assumption that larger particles are no more or less likely to aggregate. From Table 1, we would expect to miss 1.5 particles if we observe 99. Therefore, if we observe  $99 + 21.9 = 120.9$  particles, we would estimate there to be  $100.5 \times 120.9 / 99 = 122.7$  of them. In comparison, 115 particles can be counted in Fig 1, of which one is missing in Fig 2 and 15 produce the 7 grey areas.

To explore sampling variability, a further 24 digitisations of Fig 1 were analysed in the same way. The root-mean-square errors in  $\hat{\mu}$  and  $\hat{\sigma}$  about their means were 0.11 nm and 0.15 nm, respectively. These agree well with the average standard errors of 0.12 nm and 0.19 nm. Comparisons between Fig 1 and these sampled images showed the assumption to be false that all ‘L-shaped’ pixel groups (the fifth

configuration in Fig 5) were produced by single gold particles: on 17% of occasions two particles contributed. This leads to some overestimation of  $\mu$ . Simulations of groups of discs similar to Fig 1 showed that, fortuitously, this bias is approximately cancelled out by a bias in the other direction because larger groups of pixels are more likely to be connected and therefore omitted from the histogram.

### 2.3 Elliptical and polygonal sets

For shapes lacking full rotational symmetry, simple analytic results on probabilities do not seem to be obtainable. Minkowski sum and difference operators could be used to analyse the effects of lattice translations on the pixel representation of objects (Serra, 1992, p 225), but then rotations would also need to be considered. Here we resort to simulating shapes at random locations and orientations. By stratifying the sampling it proved possible to reduce the variances of the estimated probabilities. Locations of shape centres were restricted to a single square in the lattice, which was divided into a 10 by 10 subpixel grid. Orientations of shapes, which need only lie in the range 0 to  $\frac{\pi}{2}$ , were similarly divided into 10 intervals. In order to generate 1000 simulations, one location/orientation was generated from a uniform distribution within each of these 1000 strata. Variances were typically less than one quarter of what they would have been with simple random sampling.

The third column of Fig 5 shows the elliptical shapes which were found to maximise the probabilities. A problem of bias was encountered, in that the shape which was found to maximise the probability for the original set of 10000 simulations did not produce as high a probability if a second set of simulations was used. To overcome the bias, probabilities in Fig 5 were obtained using simulations independent of those used at the selection stage.

The fourth column of Fig 5 shows shapes built out of unit-sized blocks, arranged in the same configuration as the pixels. It can be seen that they sometimes have higher probabilities than the ellipses of producing the desired  $z$ , and sometimes lower ones. In particular, the probability is 82.0% for a unit-sized block. If blocks of other than integer dimensions are considered, then it is found that a square with area 0.97 maximises the probability of observing a single black pixel. The probability is 82.5%, which is only marginally less than that for a disc.

A numerical optimisation algorithm was used to search for optimal polygonal shapes. Iterations started from the above mentioned blocks, which were parametrised by locations of corners and at half-pixel spacings along each edge. Interiors of regions were determined using the parity principle (Pavlidis, 1981, chapter 8). The final column of Fig 5 shows the optimal shapes obtained. In most cases they are

little changed from the block patterns, a feature which is more likely to be due to the flatness of the probability surface than the optimality of the shapes.

## 2.4 Optimal set to produce a single pixel

It is an unsolved problem as to what set, if any, maximises the probability of observing a particular grouping of black pixels. As a first guess it would seem worthwhile to conjecture that a disc is optimal for a single pixel. However this is not the case. If a cog shape is considered, specified in polar coordinates  $(R, \theta)$  by

$$R = \begin{cases} r + \delta & \text{if } \theta \in (0, \frac{\pi}{4}), (\frac{\pi}{2}, \frac{3\pi}{4}), (\pi, \frac{5\pi}{4}) \text{ or } (\frac{3\pi}{2}, \frac{7\pi}{4}) \\ r - \delta & \text{otherwise,} \end{cases}$$

where  $r$  is the optimal disc radius, that is 0.541, and  $\delta$  is small, then

$$P_1 = 0.828 + 8(\sqrt{2} - 1)\delta^2 + O(\delta^3).$$

The  $\delta^2$  term in  $P_1$  corresponds to the shaded diamond shapes in Fig 6, which are a net gain at all orientations. Other changes in  $P_1$  at different orientations cancel out, to order  $\delta^2$ , when averaged over all orientations. Table 2 reports the probabilities, estimated from 70000 batches of 1000 simulations for a range of values of  $\delta$ , together with values predicted by the above equation. It can be seen that the approximation breaks down quite quickly, but it is clear that a disc is suboptimal.

Table 2: Probabilities of a single lattice vertex lying inside a randomly positioned cog, with teeth of depth  $2\delta$ , based on  $7 \times 10^7$  simulations at each size, together with an  $O(\delta^2)$  approximation to the probabilities.

$\delta$	$P_1$ %	$0.828 + 8(\sqrt{2} - 1)\delta^2$
0.00	82.85	82.84
0.01	82.86	82.88
0.02	82.90	82.98
0.03	82.89	
0.04	82.73	
0.05	82.11	
(se 0.003)		

### 3 Deblurring

In the previous section we inferred  $\tilde{f}$  from  $z$ . We now need to work backwards from  $\tilde{f}$  to obtain the original binary image ( $f$ ), for known background and foreground levels, threshold and blur. However, without additional information the problem is ill-posed, because there is no one-to-one correspondence between  $f$  and  $\tilde{f}$ . For example, any fine structures with measure zero in  $f$  will disappear upon blurring. Also, I know of no result which proves that every conceivable set  $\tilde{C}$  is realisable by some set  $C$ .

Discs are the easiest sets to work with and are of relevance to the interpretation of Fig 2. They will be considered in §3.1. A general algorithm for obtaining one possible  $f$ , given  $\tilde{f}$ , will be considered in §3.2, and illustrated for the case where  $\tilde{C}$  is a square.

#### 3.1 Discs

If  $C$  is a disc, then  $\tilde{C}$  will also be a disc. Fig 7 shows the relationship between  $C$  and  $\tilde{C}$  for a range of radii and thresholds at 25%, 50% and 75% of the interval between foreground and background image intensity levels. This was obtained using an algorithm for bivariate Gaussian integration over a disc given by Gilliland (1962) and Patel and Read (1982, pp 303).

For the range of disc sizes found in §2.2, and for  $\tau = 1.4$  nm and a threshold of 25%, the calibration curve is well approximated by a linear relationship in which the radius of  $C$  is

$$0.72 + 0.976r,$$

where  $r$  is the radius of  $\tilde{C}$ . Therefore, the results of §2.2 convert to a normal distribution with mean  $0.72 + 0.976 \times 5.8 = 6.4$  nm, standard deviation  $0.976 \times 0.57 = 0.56$  nm. The estimated mean agrees well with the known mean of 6.5 nm. However, the standard deviation appears to be overestimated: it should be 0.41 nm. This is probably caused by incorrectly assuming that ‘L-shaped’ groups of pixels are single particles.

#### 3.2 General sets

If we assume that  $f$  is constant over squares within a fine grid of spacing  $\Delta$ , and restrict attention to  $\tilde{f}$  on the same grid, then the problem can be formulated as

finding  $f$  such that

$$f_1 \leq f \leq f_0$$

and

$$\sum_k \sum_l f(k\Delta, l\Delta) g'(k\Delta - m\Delta, l\Delta - n\Delta) \begin{cases} \leq T & \text{if } (m\Delta, n\Delta) \in \tilde{C} \\ \geq T + \epsilon & \text{otherwise,} \end{cases}$$

where  $k, l, m$  and  $n$  are integers,

$$g'(u, v) = \int_u^{u+\Delta} \int_v^{v+\Delta} g(x, y) dx dy,$$

and  $\epsilon$  is a small positive constant. Standard linear programming algorithms exist for this problem. Strictly,  $f$  should be constrained to take values of either  $f_1$  or  $f_0$ , but this is a far-less tractable problem. In practice, at the solution most  $f(k\Delta, l\Delta)$  lie at the limits and the remainder can be dealt with by further subdivision.

Fig 8 shows possible sets ( $C$ ) at scale  $\Delta = 0.1$  pixels, which can produce squares of dimensions 1, 2 and 3 after Gaussian blurring with unit variance and thresholding at 50%. Rotational and reflection symmetries in  $\tilde{C}$  were used to reduce the number of elements to be considered. Hence the eight-fold symmetries in all the results. Corners have been built-up in a similar way to that found by Saleh (1987) and Fu *et al* (1991). These results are not unique, but identifiability could be ensured by requiring the solution to maximise a linear criterion such as the total area, in addition to satisfying the constraints.

## 4 Discussion

As common sense would suggest, inference is very uncertain from binary data to binary scenes. One exception is where an image consists of a population of well-separated objects of specified shape and size, except for one or two parameters, such as in Fig 1. However, even in this case, problems arose through interference between objects.

If observed data are multi-level rather than binary then much more progress can be made. Havelock (1989) found that grey-level quantisation led to far greater loss of information than did spatial quantisation. Kiryati and Bruckstein (1991) showed that blur improves the resolving power of digitised images. Jennison and Jubb (1991) and Hitchcock and Glasbey (1995) considered the restoration to subpixel accuracy of binary scenes containing objects only a few pixels across. Inference was found to be far more precise than that found here for binary data.

## Acknowledgements

I am grateful to Ian Roberts, Scottish Crop Research Institute, for permission to use Fig 1, and to an anonymous referee for the many helpful comments made on an earlier version of the paper. The work was supported by funds from the Scottish Office Agriculture and Fisheries Department.

## References

- Ambartzumian, R.V. (1981). *Combinatorial Integral Geometry: with Applications to Mathematical Stereology*. Wiley, Chichester.
- Aykroyd, R.G. and Green, P.J. (1991). Global and local priors, and the location of lesions using gamma-camera imagery. *Philosophical Transactions of the Royal Society, London, Series A*, **337**, 323-342.
- Bleher, P.M., Cheng, Z.M., Dyson, F.J. and Lebowitz, J.L. (1993). Distribution of the error term for the number of lattice points inside a shifted circle. *Communications in Mathematical Physics* **154**, 433-469.
- Boult, T.E. and Wolberg, G. (1993). Local image-reconstruction and subpixel restoration algorithms. *CVGIP: Graphical Models and Image Processing* **55**, 63-77.
- Bruckstein, A.M. (1987). On optimal image digitization. *IEEE Transactions on Acoustics, Speech and Signal Processing* **35** 553-555.
- Davies, E.R. (1990). *Machine Vision*. Academic Press, New York.
- Dorst, L. and Duin, R.P.W. (1984). Spirograph theory: a framework for calculations of digitized straight lines. *IEEE Transactions on Pattern Analysis and Machine Intelligence* **6**, 632-639.
- Fu, C.C., Yang, T.S. and Stone, D.R. (1991). Enhancement of lithographic patterns by using serif features. *IEEE Transactions on Electron Devices* **38**, 2599-2603.
- Gilliland, D.C. (1962). Integral of the bivariate normal distribution over an offset circle. *Journal of the American Statistical Association* **57**, 758-768.
- Grenander, U. (1976). *Pattern Synthesis: Lectures in Pattern Theory Volume 1*. Springer-Verlag, New York.

- Havelock, D.I. (1989). Geometric precision in noise-free digital images. *IEEE Transactions on Pattern Analysis and Machine Intelligence* **11**, 1065-1075.
- Havelock, D.I. (1991). The topology of locales and its effects on position uncertainty. *IEEE Transactions on Pattern Analysis and Machine Intelligence* **13**, 380-386.
- Hitchcock, D. and Glasbey, C.A. (1995). Binary image restoration at sub-pixel resolution from multi-level data. *BioSS internal report*.
- Holgate, P. (1990). Lattice points in a random parallelogram. *Advances in Applied Probability* **22**, 484-485.
- Jennison, C. and Jubb, M. (1991). Aggregation and refinement in binary image restoration. *Spatial Statistics and Imaging, IMS Lecture Notes, Hayward*, 150-162.
- Kendall, D.G. (1948). On the number of lattice points inside a random oval. *Quarterly Journal of Mathematics* **19**, 1-26.
- Kendall, M.G. and Moran, P.A.P. (1962). *Geometrical Probability*. Griffin, London.
- Kiryati, N. and Bruckstein, A.M. (1991). Gray levels can improve the performance of binary image digitizers. *CVGIP: Graphical Models and Image Processing* **53**, 31-39.
- Koplowitz, J. and Raj, A.P.S. (1987). A robust filtering algorithm for subpixel reconstruction of chain coded line drawings. *IEEE Transactions on Pattern Analysis and Machine Intelligence* **9**, 451-457.
- Korostelev, A.P. and Tsybakov, A.B. (1993). *Minimax Theory of Image Reconstruction*. Springer-Verlag, New York.
- Nakamura, A. and Aizawa, K. (1984). Digital circles. *Computer Vision, Graphics and Image Processing* **26**, 242-255.
- Nielsen, L., Astrom, K.J. and Jury, E.I. (1984). Optimal digitization of 2-D images. *IEEE Transactions on Acoustics, Speech and Signal Processing* **32**, 1247-1249.
- Patel, J.K. and Read, C.B. (1982). *Handbook of the Normal Distribution*. Marcel Dekker, New York.
- Pavlidis, T. (1981). *Algorithms for Graphics and Image Processing*. Computer Science Press, Rockville, MD.
- Ripley, B.D. (1991). The use of spatial models as image priors. *Spatial Statistics*

*and Imaging, IMS Lecture Notes, Hayward, 309-340.*

Roberts, I.M. (1994). Factors effecting the efficiency of immunogold labelling of plant virus antigens in thin sections. *Journal of Virological Methods* (in press).

Rudemo, M. and Stryhn, H. (1994). Approximating the distribution of maximum likelihood contour estimators in two-region images. *Scandinavian Journal of Statistics* (in press).

Rosenfeld, A. and Kak, A.C. (1982). *Digital Picture Processing (2nd edition)*. Academic Press, San Diego.

Saleh, B.E.A. (1987). Image synthesis: discovery instead of recovery. In *Image Recovery: Theory and Application* (ed H. Stark). Academic Press, Orlando, 463-498.

Serra, J. (1982). *Image Analysis and Mathematical Morphology*. Academic Press, London.

Serra, J. (ed.) (1988). *Image Analysis and Mathematical Morphology. Volume 2: Theoretical Advances*. Academic Press, London.

Solomon, H. (1978). *Geometric Probability*. Society for Industrial and Applied Mathematics, Philadelphia.

Sriraman, R., Koplowitz, J. and Mohan, S. (1989). Tree searched chain coding for subpixel reconstruction of planar curves. *IEEE Transactions on Pattern Analysis and Machine Intelligence* **11**, 95-103.

## Captions for figures

\*\*\* Figures 3 and 6 are missing, and some of the others lack captions \*\*\*

**Fig 1** Electron micrograph ( $1.07 \mu\text{m} \times 0.65 \mu\text{m}$ ) of section of pellet of purified tulip virus X which has been immunogold labelled with antiserum.

**Fig 2** Binary digitisation of Fig 1, at 8.5 nm per pixel. Grey regions have been used to denote groups of pixels which are the wrong shape or too big to have been produced by a single gold particle.

**Fig 3** Positions for the centre of a disc in a single square in the lattice such that 0, 1 or 2 vertices lie inside the disc, for radius ( $r$ ) in the range 0.5 to  $\sqrt{0.5}$ .

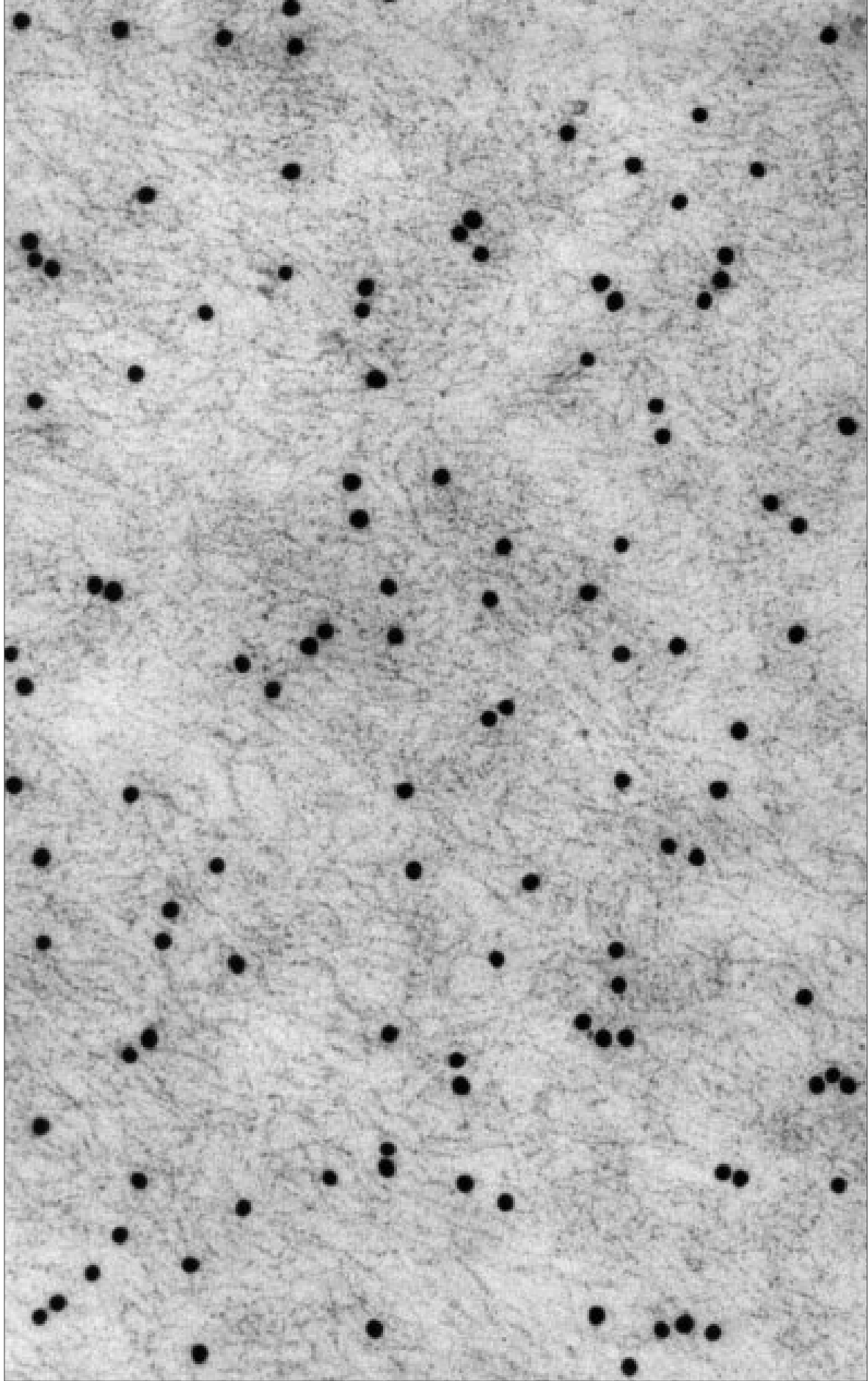
**Fig 4** Probabilities of different numbers of lattice vertices lying inside a randomly positioned disc, for a range of disc areas.

**Fig 5** Shapes which maximise the probabilities of obtaining specified patterns of pixels, together with percentage probabilities. Columns from left to right are: observed pattern, optimal sizes of discs (blank entries are where the observed pattern cannot be generated by a disc), optimal ellipses, unit-sized blocks and polygons found by a search procedure starting from the block shapes.

**Fig 6** Modification of Fig 3 if the disc is replaced by a cog shape. The shaded diamond areas are net gains to the probability of obtaining a single vertex.

**Fig 7** The relationship between the radius of disc  $C$  and the radius of disc  $\tilde{C}$  obtained by blurring  $C$  with a Gaussian density (standard deviation  $\tau$ ) and thresholding at 25%, 50% and 75% of the way between the foreground and background levels.

**Fig 8** Shapes which, after blurring and thresholding, produce squares of size 1, 2 and 3. Columns from left to right: initial shapes, shapes after blurring, and shapes after blurring and thresholding.



15

Fig 1

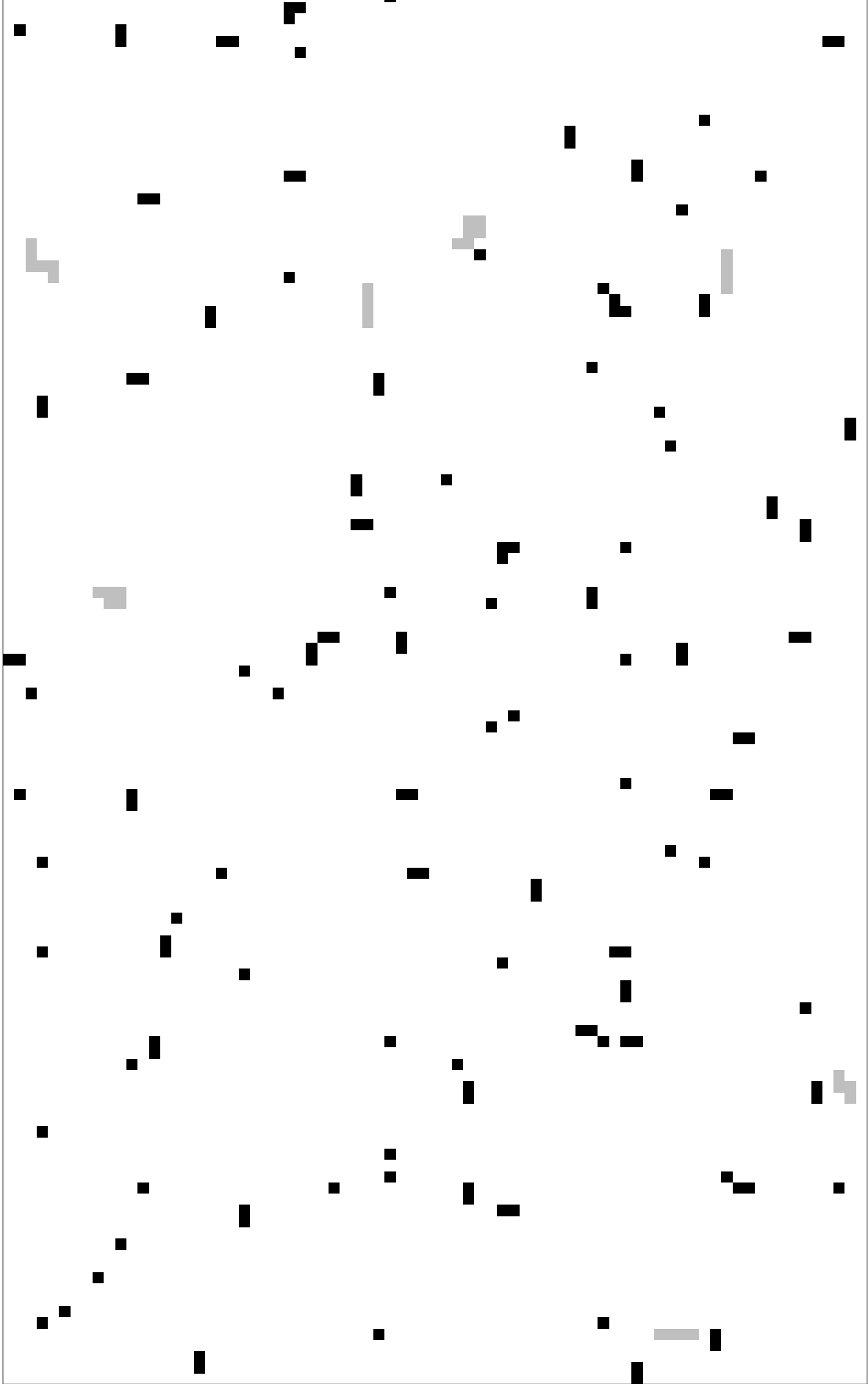


Fig 2

Fig 4

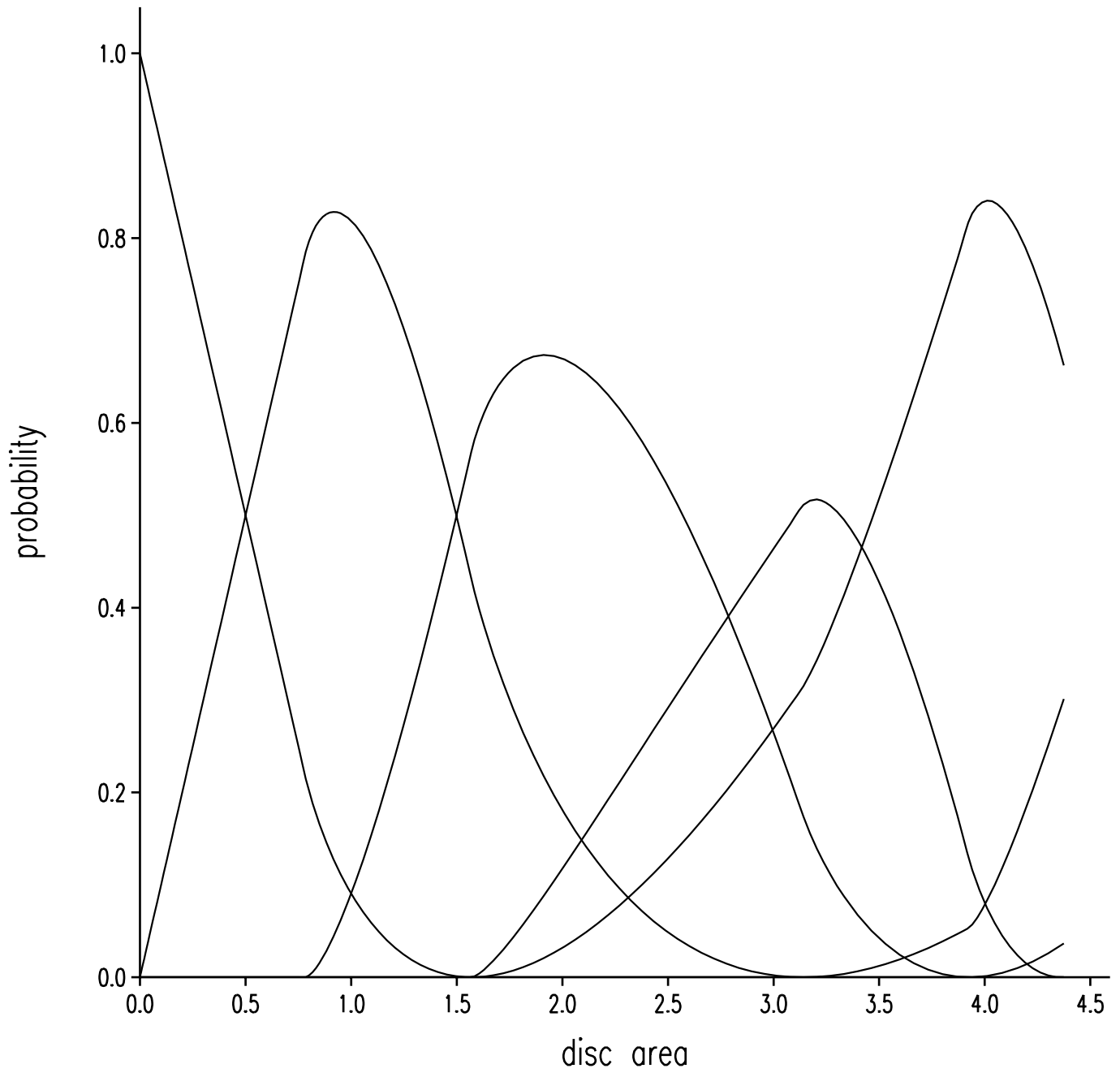
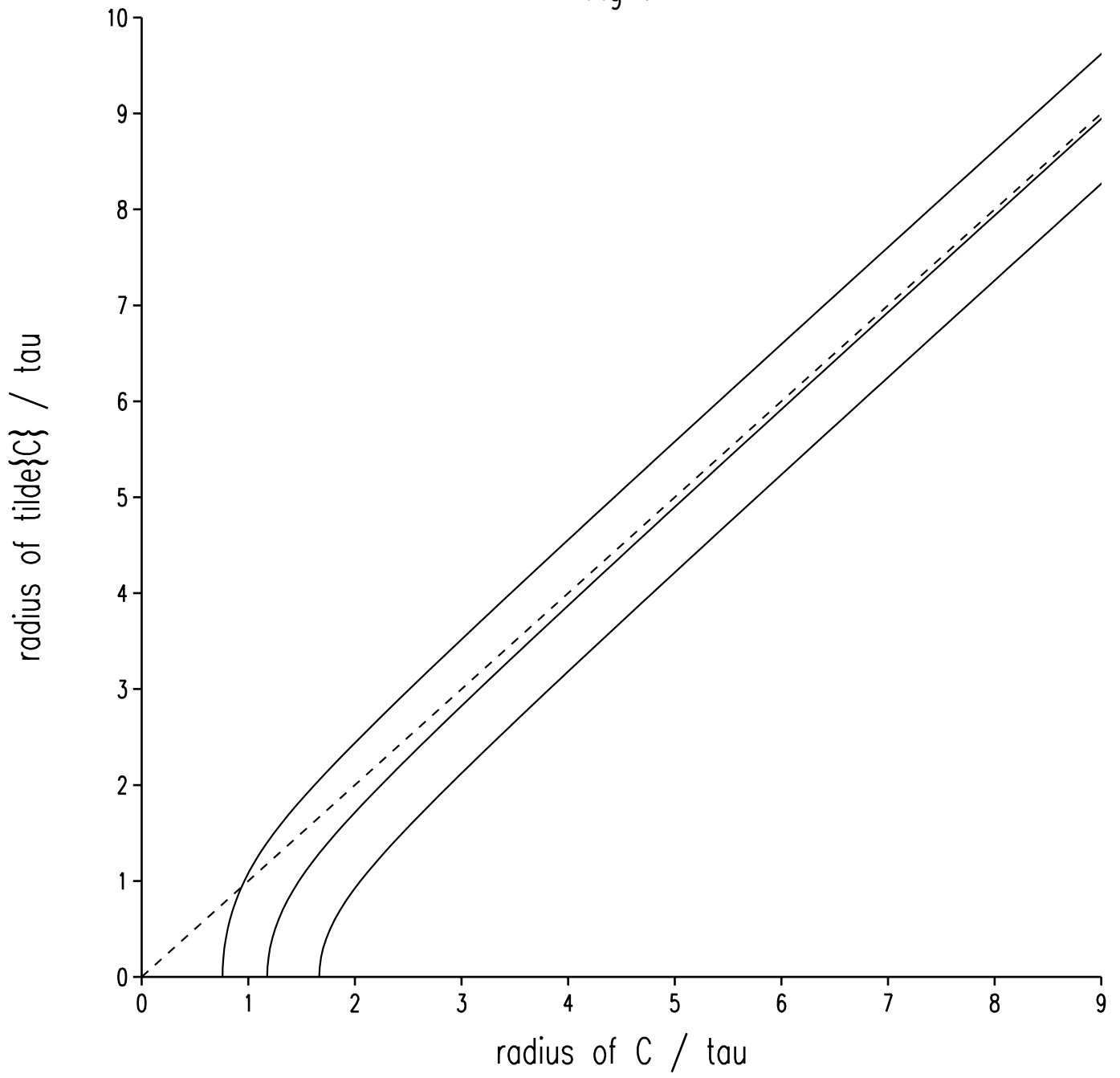




Fig 7



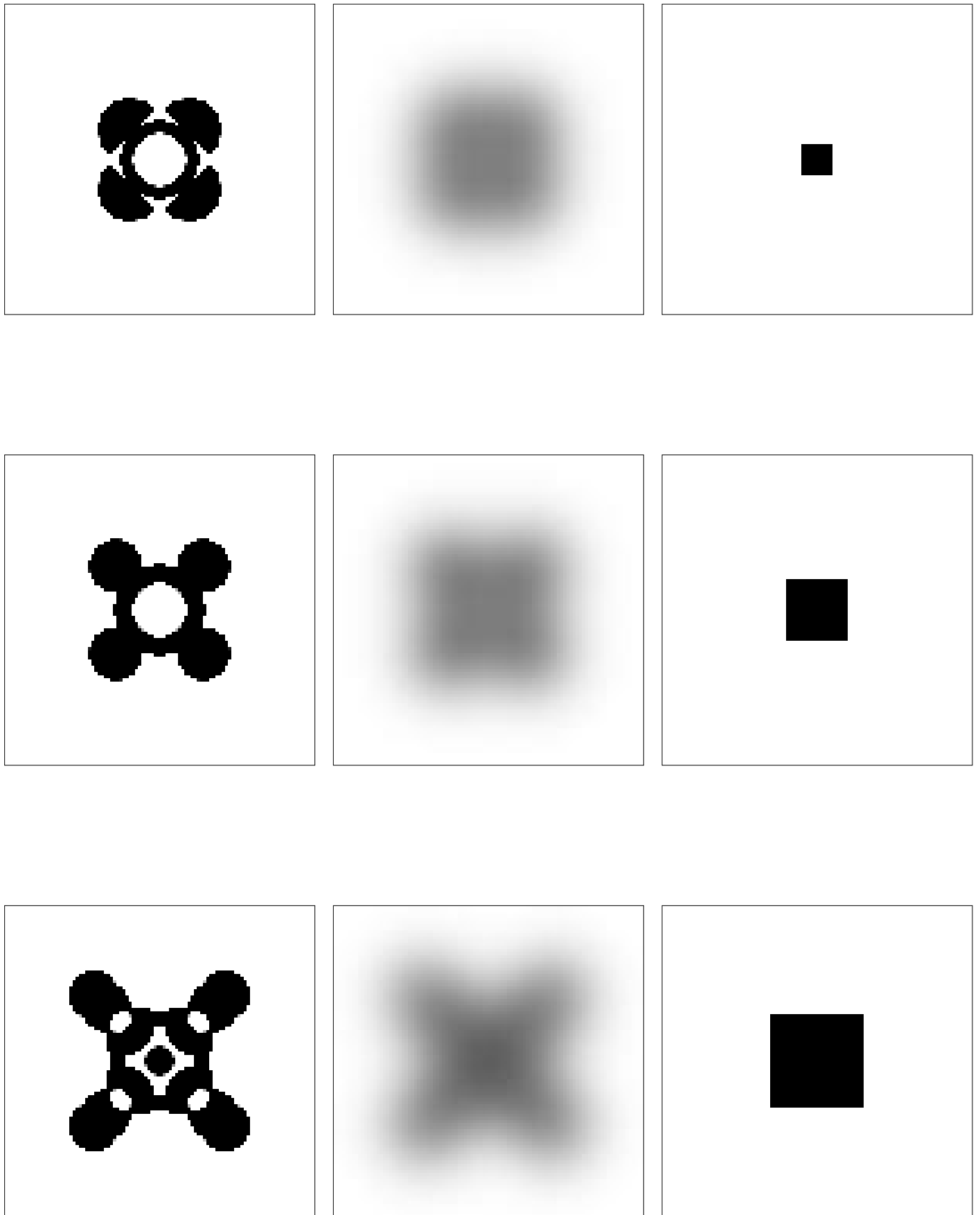


Fig 8